Ab initio calculation of the whole set of He double-photoionization cross sections

P. Selles and L. Malegat
Laboratoire de Spectroscopie Atomique et Ionique (Laboratoire Associé au CNRS), Université Paris–Sud, Batiment 350, 91405 Orsay Cedex, France

A. K. Kazansky
Fock Institute of Physics, The University of St. Petersburg, St. Petersburg 198504, Russia
(Received 6 June 2001; published 13 February 2002)

The double photoionization of He is investigated using the hyperspherical $\mathcal{R}$ matrix with semiclassical outgoing waves method. Triply, doubly, and singly differential, as well as fully integrated, cross sections are computed in a variety of geometrical and dynamical situations. The results are found to be in excellent agreement with absolute measurements both in shape and, more importantly, in magnitude. This demonstrates the robustness and accuracy of this *ab initio* method, which also provides a visualization of the formation of the various cross sections during the expansion of the system. This visualization reveals that, for very asymmetric energy sharings, the cross sections take their final form when the electrons are thousands of atomic units away from the ionic core, a distance where no other method is able to describe the double continuum wave function accurately.

DOI: 10.1103/PhysRevA.65.032711 PACS number(s): 32.80.Fb

I. INTRODUCTION

Double photoionization of atoms by one photon has become a ''hot topic'' in the last ten years. This is due, first, to a great increase in the intensity of highly monochromatic synchrotron radiation with well-defined polarization properties, and, second, to the development of powerful detection techniques which are capable of simultaneously collecting electrons over a wide range of angles and energies. Experiments performed in the last decade [1–13] have produced a large amount of information that is challenging to theory. Despite the theoretical advances that have been made in this field over the same time scale [14–19], attempts to calculate accurate differential cross sections have, in our view, yielded disappointing results, although some recent developments seem very promising [20,22]. In this paper, we present a theory which is capable of calculating accurate values for the absolute differential cross sections associated with double photoionization of the helium atom.

Theoretical studies of the processes related with the two-electron continuum started with the well-known paper by Wannier [23], which soon will celebrate its 50th anniversary. In that paper, Wannier deduced the threshold law for double-electron escape from an ingenious analysis of the classical equations of motion of the two electrons far from the nucleus. After Wannier's success, the theoretical interest in the problem remained quite moderate for decades. Twenty years later, at last, his result was confirmed by the numerical calculations of Vinkalns and Gailitis [24], and one element of his analysis started to inspire developments in the field: namely, the dominant contribution of symmetric back-to-back emisssion to the near-threshold double escape. Then, for years, investigations concentrated on the quantum or semiclassical analysis of the system within a quadratic approximation for the potential in the vicinity of the so-called Wannier configuration $\vec{r}_1 \approx -\vec{r}_2$ [25–27].

During the 1990s, the rate of development of theoretical methods in the field increased very rapidly. An attempt to go beyond the above-mentioned quadratic approximation was undertaken by Kazansky and Ostrovsky. Their extended Wannier ridge model (EWRM) [19] revealed the inconsistency of that approximation, at least as far as the angular distribution of the electrons is concerned, and gave qualitative ideas regarding the role of electron correlation in forming angular patterns under equal energy sharing conditions. However, EWRM could not be reliably applied to the system in the vicinity of the nucleus, and this put the calculation of accurate values of the cross sections beyond its reach. Meanwhile, the 3 Coulomb waves (3C) approach [14] together with the convergent close coupling (CCC) method [15] provided extensive sets of triply differential cross sections (TDCS), which have been compared with experimental data with varying degrees of success. 3C has a phenomenological character that qualifies it as a convenient and flexible tool to get insights into the double-escape process, but not as a reliable method to compute accurate cross sections, notably because its gauge dependence is too important. CCC implies that electron-electron correlations are neglected at large distances from the core, an approximation that undermines the predictive power of this method, giving rise to a complex pattern of successes and failures that is now well documented [28]. As a result, neither method was able to obtain accurate absolute values of the entire set of cross sections associated with the double-photoionization process [29]. The 2 screened Coulomb waves (2SC) method [16–18] came closer to this goal although it was later abandoned possibly due to computational difficulties. In this respect, it should be noted that this method could be implemented only in the velocity gauge, and that it relied upon the Padé summation of a divergent series, which is a widely used, but rather uncontrolled, technique [30].

More recently, two methods have appeared, which both rely upon intense parallel computing, and seem to offer great potential. For the time being, however, the time-dependent

close coupling (TDCC) method [20] has only produced the ratio of double-to-single total photoionization cross sections.[1] On the other hand, the exterior complex scaling (ECS) method [22] has only been applied to electron-impact single ionization. In this situation, the present contribution appears as very timely. The theory proposed in this paper actually provides the entire set of absolute cross sections for the double photoionization of He over a broad range of photon energies and for arbitrary sharing of the excess energy above threshold between the two electrons. Moreover, it does so with only moderate computational efforts, while providing an instructive insight into the dynamics of the process.

Our method consists of merging two different approaches: the hyperspherical $\mathcal{R}$-matrix treatment of the two-electron system in the vicinity of the nucleus, and the semiclassical description of the evolution of the system with the hyperspherical radius R throughout the external region. We call it accordingly the hyperspherical $\mathcal{R}$ matrix with semiclassical outgoing waves (H$\mathcal{R}$M-SOW) method. The advantages of the $\mathcal{R}$-matrix approach [31] are well known: (i) it is exact, so that the accuracy of the results can be improved systematically up to any prescribed level; (ii) the processing of series of energies is quick due to the analytical energy dependence of the matrix $\mathcal{R}$; and (iii) the method benefits from all computational advances achieved within the wide domain of bound-state calculations. The semiclassical treatment of the system in the external region, based on the experience acquired within EWRM [19], also has very specific advantages: (i) from the computational point of view, it leads to a conventional propagation problem that can be solved very efficiently using a stable and unitary algorithm; and (ii) from the heuristic point of view, it allows one to vizualize the evolution of the wave function with the hyperspherical radius R (or a related mock-time τ) throughout the external region.

H$\mathcal{R}$M-SOW was formulated in 1999, and at this time, it was applied to a model double-photoionization problem, where the electronic motion was restricted to the Wannier ridge $r_1=r_2$ [32]. The possibility of applying this method to the real six-dimensional physical problem was demonstrated in 2000 [33]. Here we give a detailed account of H$\mathcal{R}$M-SOW in its latest stage of development. In Sec. II, we establish the relations between our computed wave function and the experimentally measured cross sections. In Sec. III, we reiterate the basic ideas of our $\mathcal{R}$-matrix approach, complemented with the semiclassical outgoing wave condition, which allows us to extract the wave function at the border, $R=R_0$, of the inner region. In Sec. IV, we give a detailed description of the semiclassical method we use to propagate the wave function from R_0 to the very large R values where the cross sections are extracted. In Sec. V, we present a wide selection of our results, including TDCS, angular asymmetry parameters (β) associated with doubly differential cross sections (DDCS), singly differential cross sections (SDCS), and integrated cross sections (ICS), in comparison with the experimental data. We also present the evolution of selected cross sections with the hyperradius R to illustrate the rate of redistribution of the total flux between the different outgoing channels. In Sec. VI, we summarize the main results of the present paper and outline the possible developments of our method in the future. Atomic units are used hereafter unless otherwise stated.

II. BASIC NOTIONS AND EQUATIONS

The basic formulation of the one-photon ionization problem requires solving the inhomogeneous equation

$$(\mathcal{H}_0-E)\Phi_1(\vec{r}_1,\vec{r}_2)=-\frac{1}{2}\vec{\mathcal{E}}_0\cdot\vec{D}_G\Psi_0(\vec{r}_1,\vec{r}_2) \tag{1}$$

for the stationary two-electron wave function $\Phi_1(\vec{r}_1,\vec{r}_2)$ obtained within the rotating-wave approximation. We denote the ground-state wave function and energy of the two-electron Hamiltonian $\mathcal{H}_0$ by $\Psi_0(\vec{r}_1,\vec{r}_2)$ and E_0, respectively, the frequency of the incident light by ω, and the total energy by $E=E_0+\omega$. $\vec{\mathcal{E}}_0$ is the amplitude of the electric-field vector $\vec{\mathcal{E}}(t)=\vec{\mathcal{E}}_0\cos\omega t$, and $\vec{D}_G$ is the dipole operator. The expressions for $\vec{D}_G$ in the length, velocity, and acceleration gauge read

$$\vec{D}_L=\vec{r}_1+\vec{r}_2, \tag{2a}$$

$$\vec{D}_V=\frac{1}{\omega}\left(\frac{\vec{r}_1}{r_1}\frac{\partial}{\partial r_1}+\frac{\vec{r}_2}{r_2}\frac{\partial}{\partial r_2}\right), \tag{2b}$$

$$\vec{D}_A=\frac{Z}{\omega^2}\left(\frac{\vec{r}_1}{r_1^3}+\frac{\vec{r}_2}{r_2^3}\right). \tag{2c}$$

Equation (1) has to be complemented with the outgoing wave condition imposed on the wave-function $\Phi_1(\vec{r}_1,\vec{r}_2)$. The implementation of this boundary condition is well known to be the main difficulty of the problem. It is noteworthy that the wave-function $\Phi_1(\vec{r}_1,\vec{r}_2)$ asymptotically contains contributions from the entire set of ionization channels, which includes the single-ionization channels with and without excitation of the residual ion, as well as the double-ionization channel.

We consider the problem within the hyperspherical coordinate system. The latter is composed of the hyperradius

$$R=\sqrt{r_1^2+r_2^2}, \tag{3}$$

the hyperangle

$$\alpha=\arctan(r_1/r_2), \tag{4}$$

together with the set (Ω_1,Ω_2), where Ω_1 and Ω_2 stand for the spherical angles (ϑ_1,φ_1) and (ϑ_2,φ_2) associated with the ejection directions of the two electrons. In the following, we will denote by Ω_5 the set $(\alpha,\Omega_1,\Omega_2)$ which collects the five angular variables of the problem.

[1] Recently differential cross sections for double photoionization of He have been obtained using this method [21].

The hyperspherical coordinates are known to be very convenient for the description of the various decay channels of atomic or molecular complexes. They are particularly suitable here since (i) their collective character is well adapted to the description of a correlated motion; (ii) only one variable, R, goes to ∞, which simplifies the computational task significantly; (iii) the introduction of R makes it easy to compute the cross sections directly from their very definition, based on the flux of the wave function through an hypersphere of large hyperradius $R_{\max}$; and (iv) the introduction of the variable α allows one to discriminate single ionization against double ionization. The ratio of double ionization to single ionization being no more than 2%, disentangling the weak double-ionization process from the much stronger single-ionization process to which it is tightly coupled, is a real challenge indeed. However, it can be faced easily within the hyperspherical coordinate set. Namely, when R gets large enough, single ionization becomes confined within two intervals of width $\Delta\alpha = r_{n_{\max}}/R$ around $\alpha=0$ and $\pi/2$, where $r_{n_{\max}} \simeq (0.75 n_{\max}^2)$ a.u. measures the extension of the highest Rydberg state $\mathrm{He}^+_{n=n_{\max}}$ that can be excited significantly in the one-photon absorption considered. According to the recent compilation of experimental data by Bizau and Wuillemier [34], single ionization to Rydberg states with $n>3$ accounts for less than 1% of the total single ionization cross section in the 0–80 eV energy range, so that $n_{\max} \simeq 10$ can be considered as a reasonable order of magnitude. Using this value, we obtain $\Delta\alpha = 0.075$ rad at $R=10^3$ a.u., for instance, and $\Delta\alpha \to 0$ rad as $R \to \infty$, when all single-ionization channels collapse to the points $\alpha=0$ and $\alpha=\pi/2$. In this limit, any information regarding the double-ionization process, extracted at $\alpha \neq 0, \pi/2$, is free of contamination by the dominant single-ionization channels.

Regarding the TDCS, it is important to realize that the two distinct configurations $(\alpha, \Omega_1, \Omega_2)$ and $(\pi/2 - \alpha, \Omega_2, \Omega_1)$ on the hypersphere $R = R_{\max}$ correspond to the same experimental event: one electron with energy $E_1 = E(\sin\alpha)^2$ is registered in the direction Ω_1 in coincidence with the other electron, with energy $E_2 = E - E_1$, being registered in the direction Ω_2. Accordingly, the number of events per second $d^{(3)}N(E_1, \Omega_1, \Omega_2)$, when one electron is ejected with energy $E_1 (dE_1)$ in the direction $\Omega_1 (d\Omega_1)$ and simultaneously the other electron flies out in the direction $\Omega_2 (d\Omega_2)$, is given by the sum of the fluxes through elementary surfaces surrounding these two configurations. Due to the invariance of the orbital part of the singlet wave function with respect to the exchange of the two electrons, these two fluxes are equal. Hence,

$$d^{(3)}N(E_1, \Omega_1, \Omega_2) = 2 \lim_{R\to\infty} \mathcal{F}_R(R; \Omega_5) dS_5, \tag{5}$$

where the five-dimensional surface element dS_5 around $\Omega_5 = (\alpha, \Omega_1, \Omega_2)$ is

$$\begin{aligned} dS_5 &= R^5 (\sin\alpha \cos\alpha)^2 d\alpha\, d\Omega_1 d\Omega_2 \\ &= \frac{R^5}{4E} \sin 2\alpha\, dE_1 d\Omega_1 d\Omega_2, \end{aligned} \tag{6}$$

and the hyperradial component of the flux vector, $\mathcal{F}_R(R; \Omega_5)$, is given by

$$\mathcal{F}_R(R; \Omega_5) = \frac{1}{2\imath} \left(\Phi_1^*(R; \Omega_5) \frac{\partial \Phi_1(R; \Omega_5)}{\partial R} - \Phi_1(R; \Omega_5) \frac{\partial \Phi_1^*(R; \Omega_5)}{\partial R} \right). \tag{7}$$

The TDCS is defined as

$$\frac{d^{(3)}\sigma}{dE_1 d\Omega_1 d\Omega_2} = \frac{1}{\mathcal{F}_{\mathrm{phot}}} \frac{d^{(3)}N}{dE_1 d\Omega_1 d\Omega_2}, \tag{8}$$

where the incident photon flux is

$$\mathcal{F}_{\mathrm{phot}} = \frac{c\mathcal{E}_0^2}{8\pi\omega}, \tag{9}$$

c being the velocity of light. Substituting of Eqs. (5)–(7) and (9) into Eq. (8) results in the following expression of the TDCS:

$$\frac{d^{(3)}\sigma}{dE_1 d\Omega_1 d\Omega_2} = \frac{1}{2E\mathcal{F}_{\mathrm{phot}}} \mathrm{Im} \left(\lim_{R\to\infty} R^5 \sin 2\alpha \times \left(\Phi_1^* \frac{\partial \Phi_1}{\partial R} \right) \Bigg|_{\alpha = \arcsin(\sqrt{E_1/E})} \right). \tag{10}$$

The other measurable quantities, which can be directly obtained from the TDCS, are the doubly differential cross section (DDCS)

$$\frac{d^{(2)}\sigma}{dE_1 d\Omega_1} = \int d\Omega_2 \frac{d^{(3)}\sigma}{dE_1 d\Omega_1 d\Omega_2}, \tag{11}$$

the singly differential cross section (SDCS)

$$\frac{d^{(1)}\sigma}{dE_1} = \int d\Omega_1 \int d\Omega_2 \frac{d^{(3)}\sigma}{dE_1 d\Omega_1 d\Omega_2}, \tag{12}$$

and the integrated cross section (ICS)

$$\sigma^{++} = \int_{0^+}^{E/2} dE_1 \int d\Omega_1 \int d\Omega_2 \frac{d^{(3)}\sigma}{dE_1 d\Omega_1 d\Omega_2}. \tag{13}$$

The symbol 0^+ at the lower energy-integration limit recalls that integration has to exclude the singular point $\alpha=0$ to which all single-ionization channels collapse in the limit $R \to \infty$. The well-known relationship

$$\sigma^{++} = \int_{0^+}^{E/2} dE_1 \frac{d^{(1)}\sigma}{dE_1} \tag{14}$$

between the ICS and the SDCS follows from Eqs. (12) and (13). It is noteworthy that restricting the energy integration to half the total energy interval in Eqs. (13) and (14) avoids double counting of the same double-photoionization event. Also note that the factor 2 in Eq. (5) compensates for the

division by 2 of the energy interval of integration in Eqs. (13) and (14) so that σ^{++} is given alternatively by

$$\sigma^{++}=\frac{1}{\mathcal{F}_{\mathrm{phot}}}\lim_{R\to\infty}\int_{0^+}^{(\pi/2)^-}d\alpha\int d\Omega_1\int d\Omega_2 R^5 \times(\sin\alpha\cos\alpha)^2\mathcal{F}_R(R;\alpha,\Omega_1,\Omega_2), \tag{15}$$

that is to say, by the ratio of the total outgoing flux to the incoming photon flux, excluding the vicinity of $\alpha=0$ and $\alpha=\pi/2$. If this exclusion is relieved, then the total ionization cross section $\sigma^{+}+\sigma^{++}$ is obtained.

III. EXTRACTION OF THE SOLUTION AT R_0

Let us introduce the function

$$\Phi(R;\Omega_5)=R^{5/2}\sin 2\alpha\Phi_1(R;\Omega_5), \tag{16}$$

and rewrite Eq. (1) more explicitly for this function as

$$\left(-\frac{1}{2}\frac{\partial^2}{\partial R^2}+\frac{1}{2}\frac{\mathcal{T}(\Omega_5)}{R^2}-\frac{1}{8R^2}+\frac{\mathcal{V}(\Omega_5)}{R}-E\right)\Phi(R;\Omega_5) =\Phi^G(R;\Omega_5). \tag{17}$$

The inhomogeneous term is given by

$$\Phi^G(R;\Omega_5)=-\frac{1}{2}R^{5/2}\sin 2\alpha(\vec{\mathcal{E}}_0\cdot\vec{D}_G)\Psi_0(R;\Omega_5), \tag{18}$$

and the angular kinetic-energy operator $\mathcal{T}(\Omega_5)$ is

$$\mathcal{T}(\Omega_5)=-\frac{\partial^2}{\partial\alpha^2}+\frac{l_1^2}{(\sin\alpha)^2}+\frac{l_2^2}{(\cos\alpha)^2}, \tag{19}$$

where $\vec{l}_1$ and $\vec{l}_2$ are the orbital angular momenta of the two electrons. The potential operator $\mathcal{V}(\Omega_5)$ is the sum of the electron-nucleus (en) and electron-electron (ee) interactions

$$\mathcal{V}(\Omega_5)=\mathcal{U}_{\mathrm{en}}(\alpha)+\mathcal{U}_{\mathrm{ee}}(\Omega_5), \tag{20a}$$

$$\mathcal{U}_{\mathrm{en}}(\alpha)=-Z\cos\alpha-Z\sin\alpha, \tag{20b}$$

$$\mathcal{U}_{\mathrm{ee}}(\Omega_5)=\frac{1}{\sqrt{1-\sin 2\alpha\cos\theta_{12}}}, \tag{20c}$$

where Z is the charge of the nucleus ($Z=2$ for He), and θ_{12} is the angle between the ejection directions of the two electrons.

We obtain the wave function on the hypersphere $R=R_0$ which separates the inner region from the outer region by completing successively the five following tasks:

(1) Solving the $\mathcal{R}$-matrix eigenvalue equation

$$\left(-\frac{1}{2}\frac{\partial^2}{\partial R^2}+\frac{1}{2}\delta(R-R_0)\frac{\partial}{\partial R}+\frac{1}{2}\frac{\mathcal{T}(\Omega_5)}{R^2}-\frac{1}{8R^2} +\frac{\mathcal{V}(\Omega_5)}{R}-\epsilon_k\right)\Phi^k(R;\Omega_5)=0, \tag{21}$$

which is obtained from Eq. (17) by omitting the inhomogeneous term and by adding the Bloch operator to the Hamiltonian in order to ensure that it is Hermitian over the finite inner region $R\leqslant R_0$.

(2) Evaluating the local operator $\mathcal{I}_{R_0}(\Omega_5)$ and the nonlocal operator $\mathcal{R}_{R_0}(\Omega_5,\Omega_5')$,

$$\mathcal{I}_{R_0}(\Omega_5)=\sum_k\frac{\langle\Phi^k|\Phi^G\rangle}{\epsilon_k-E}\Phi^k(R_0;\Omega_5), \tag{22a}$$

$$\mathcal{R}_{R_0}(\Omega_5,\Omega_5')=\frac{1}{2}\sum_k\frac{\Phi^k(R_0;\Omega_5)\Phi^{k*}(R_0;\Omega_5')}{\epsilon_k-E}. \tag{22b}$$

(3) Calculating the eigenvectors $X_\lambda(R_0;\Omega_5)$ and eigenvalues $E_\lambda(R_0)$ of the fixed $R=R_0$ Hamiltonian by solving

$$\left(+\frac{1}{2}\frac{\mathcal{T}(\Omega_5)}{R_0^2}-\frac{1}{8R_0^2}+\frac{\mathcal{V}(\Omega_5)}{R_0}-E_\lambda(R_0)\right)X_\lambda(R_0;\Omega_5)=0. \tag{23}$$

(4) Solving the set of $\mathcal{R}$-matrix equations

$$F_\lambda(R_0)=\sum_{\lambda'}\overline{\mathcal{R}}_{\lambda\lambda'}(R_0)F'_{\lambda'}(R_0)+\overline{\mathcal{I}}_\lambda(R_0), \tag{24}$$

complemented with the semiclassical relation

$$F'_\lambda(R_0)=\imath p_\lambda(R_0)F_\lambda(R_0), \tag{25}$$

for the hyperradial channel functions $F_\lambda(R_0)$ defined by

$$\Phi(R_0;\Omega_5)=\sum_\lambda F_\lambda(R_0)X_\lambda(R_0;\Omega_5). \tag{26}$$

The $\overline{\mathcal{I}}_\lambda(R_0)$ vector and the $\overline{\mathcal{R}}_{\lambda\lambda'}(R_0)$ matrix result from expanding the local operator $\mathcal{I}_{R_0}(\Omega_5)$ and the nonlocal operator $\mathcal{R}_{R_0}(\Omega_5,\Omega_5')$ over the basis $X_\lambda(R_0;\Omega_5)$. The semiclassical momenta $p_\lambda(R_0)$ are given by

$$p_\lambda(R_0)=\sqrt{2[E-E_\lambda(R_0)]}\quad\text{for}\quad E>E_\lambda(R_0), \tag{27a}$$

$$p_\lambda(R_0)=\imath\sqrt{2[E_\lambda(R_0)-E]}\quad\text{for}\quad E\leqslant E_\lambda(R_0). \tag{27b}$$

(5) Assembling the wave function $\Phi(R_0;\Omega_5)$ at the boundary R_0 according to Eq. (26).

The scheme proposed above includes three approximations, which underlie Eq. (25). First, we assume that the R dependence of the local angular vectors $X_\lambda(R;\Omega_5)$ can be neglected within a small interval $[R_0,R_0+\delta R_0]$. Within this *adiabatic* approximation, the associated hyperradial channel functions are uncoupled, and their evolution is governed by the adiabatic potentials $E_\lambda(R)$ [35]. Second, we replace each channel function by its *semiclassical* approximation using the local momentum defined by Eq. (27). Third, we impose the *outgoing wave condition at* $R=R_0$, by suppressing incoming contributions as shown by Eq. (25). Note that our approach requires the adiabatic and semiclassical approxima-

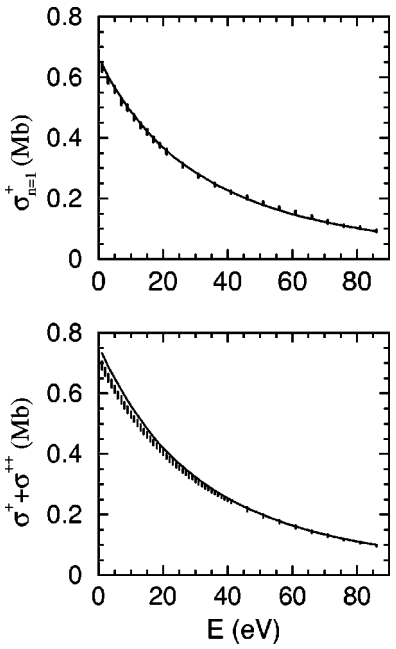

FIG. 1. Top panel: total cross section for single ionization of He without excitation, in Mb, versus the energy, in eV, measured with respect to the double-ionization threshold. Dots with error bars: experimental data compilation by Bizau and Wuillemier [34]. Solid line: present calculations (length, velocity, and acceleration are superimposed). Bottom panel: total photoionization cross section of He, in Mb, versus the energy, in eV, measured as on top panel. Dots with error bars: experiment by Samson *et al.* [4]. Solid lines: present calculations (length, velocity, and acceleration are superimposed).

tions to be valid only in the small interval $[R_0, R_0+\delta R_0]$ that has to be considered for computing the first derivatives of the channel functions. This is why one expects these two approximations to be nonrestrictive. By contrast, it is not obvious that imposing the outgoing wave boundary condition at R_0 is valid, given the small value of R_0 used in the present calculations, where $R_0=10$ a.u.

One way to check this is to compute the total outgoing flux of the resulting $\Phi_1(R_0;\Omega_5)$ through the hypersphere $R=R_0$ and to divide it by the incoming photon flux to obtain the total ionization cross section

$$\sigma^+ + \sigma^{++} = \frac{2\pi\omega}{c\mathcal{E}_0^2} \sum_{E_\lambda \leqslant E} p_\lambda(R_0) |F_\lambda(R_0)|^2. \qquad (28)$$

The lowest adiabatic energy $E_{\lambda=0}(R_0)$ being very close to that of one free electron a distance R_0 away from the He^+ ion in its ground-state $n=1$, we identify the corresponding adiabatic state to the lowest single-ionization channel, and obtain the associated cross section accordingly as

$$\sigma^+_{n=1} = \frac{2\pi\omega}{c\mathcal{E}_0^2} p_0(R_0) |F_0(R_0)|^2. \qquad (29)$$

The results are shown in Fig. 1. On the top panel, the computed single-ionization cross section to the ground state of He^+ is in excellent agreement with the most recent compilation of experimental results by Bizau and Wuillemier [34] over the entire energy range. This proves that the channel corresponding to single ionization to the ground state of He^+ is definitely decoupled from all other ionization channels at $R=R_0$. At this distance, by contrast, these other channels remain closely coupled together. The figure also shows that the lowest single-ionization channel can be accounted for very accurately by imposing the outgoing wave boundary condition at R_0. On the bottom panel, the agreement between the calculated total ionization cross section and the acknowledged reference experiment of Samson *et al.* [4] is also very good, although it deteriorates as energy decreases. The computed values are within the experimental error bars from 30 eV upwards, the computed value at 20 eV is within 2% of experiment, and that obtained at 1 eV is still within 12% of the experimental value. This demonstrates that imposing the outgoing wave boundary condition at $R_0=10$ a.u. remains a good approximation for single ionization with excitation and double ionization. However, to make it very good down to the few electron volt range, an increase of R_0 is clearly needed. Note that our method is designed especially to treat electron-electron correlations nonperturbatively, so that its relevant domain of application is the low-to-intermediate energy range where these correlations are important. Perturbative methods do well enough at higher energies. This is why we have not pushed our investigation beyond 86 eV.

The implementation of the scheme described above requires a convenient representation of the vectors $\Phi^k(R;\Omega_5)$ and $X_\lambda(R;\Omega_5)$, the choice of which is guided by the known $^1P^o$ symmetry of the final photoabsorption state with $S=0$, $L=1$, and $M=0,\pm 1$, depending on the polarization of the incident light. The representation we use here is based on the bipolar spherical harmonics $\mathcal{Y}^{1M}_{l,l+1}(\Omega_1,\Omega_2)$ [36], or, more precisely, on their gerade (g) and ungerade (u) combinations ${}^g_u\mathcal{Y}^{1M}_{l,l+1}(\Omega_1,\Omega_2)$, which are, respectively, symmetric and antisymmetric in the exchange of the two electrons. These functions are complemented with trigonometric functions of multiples of the angle α, and with a Lagrange mesh [37] representation for the variable R. The technical details are documented in the Appendix. Here, we only wish to stress a few important properties of this representation.

First, it leads to a numerical task light enough to be completed on a plain PC (Pentium III 450 MHz, 768 Mb RAM).

Second, it is accurate enough numerically to ensure the gauge invariance of our results. Namely, each solid line on Fig. 1 is threefold: it results from the superposition of the results we obtain in the length, velocity, and acceleration gauges, which cannot be distinguished at the scale of the figure.

Third, it provides an accurate representation of the dynamics that takes place within the inner region $R \leqslant R_0$. This is demonstrated by the very good values that we obtain for the energies of well known $^1P^o$ excited bound states of He. Namely, at energies below the lowest adiabatic energy $E_{\lambda=0}(R_0)$, Eqs. (25) and (27b) impose an exponentially decaying behavior in all channels. This is the appropriate boundary condition for bound states. The bound-state ener-

gies then appear as sharp resonances in the energy dependence of any component $F_\lambda(R_0)$ of the solution of the system formed by Eqs. (24) and (25). Given $E_{\lambda=0}(R_0) = -2.083$ a.u., the bound-state boundary condition is fulfilled in the energy region of the first singly excited $^1P^o$ state of He, which is known to lie at -2.124 a.u. [38]. Our calculated value is -2.122 a.u. The second singly excited $^1P^o$ state lies around -2.055 a.u. [38], that is to say above the first adiabatic energy, and therefore we cannot obtain it by the simple procedure outlined above. By contrast, the boundary condition is fulfilled for the first doubly excited $^1P^o$ state, although it also lies above the first adiabatic energy, because it is orthogonal to the corresponding adiabatic state. We obtain for its position -0.693 a.u., in excellent agreement with the tabulated value of -0.694 a.u. [38].

IV. SEMICLASSICAL PROPAGATION OF THE WAVE FUNCTION IN THE EXTERNAL REGION

We now consider solving Eq. (17) in the outer region. Our previous computation of the wave function at R_0 will provide us with the required boundary condition. The inhomogeneous term is proportional to the short-range ground-state wave function of He [see Eq. (18)], and so it can be neglected. It follows that no gauge dependence can appear in the outer region, so that the results obtained at $R=R_0$ will keep their gauge-invariance property throughout the external region. We consider the problem within a semiclassical outgoing wave approximation consistent with that used in the calculation of $\Phi(R_0;\Omega_5)$. It takes the form

$$\Phi(R;\Omega_5)=\frac{1}{\sqrt{p(R)}}\exp\left(\imath\int_{R_0}^{R}p(R')dR'\right)\tilde{\Phi}(R;\Omega_5), \tag{30}$$

suggested by the experience acquired within EWRM [19]. The above ansatz presupposes that the hyper-radial motion can be described approximately in terms of a unique local momentum $p(R)$. This contrasts with the semiclassical outgoing wave approximation we used to extract $\Phi(R_0;\Omega_5)$, which relay upon channel-dependent local momenta $p_\lambda(R)$. The local momentum we use here is given by

$$p(R)=\sqrt{2\left(E+\frac{Z_{\rm eff}(R)}{R}\right)}, \tag{31}$$

where the effective charge $Z_{\rm eff}(R)$ is a rational interpolation, involving a single parameter η, between the asymptotic value, which is taken equal to the Wannier charge $Z_W=(4Z-1)/\sqrt{2}$, and the value at R_0,

$$Z_{\rm eff}(R)=Z_W\frac{\eta(R-R_0)^2}{1+\eta(R-R_0)^2}+Z_{\rm eff}(R_0) \times\left(1-\frac{\eta(R-R_0)^2}{1+\eta(R-R_0)^2}\right). \tag{32}$$

The effective charge at R_0 is obtained from the boundary condition

$$\Phi(R_0;\Omega_5)=\sum_{E_{\lambda=0}<E_\lambda\leqslant E}F_\lambda(R_0)X_\lambda(R_0;\Omega_5) \tag{33}$$

by identifying the norms and fluxes of the two expressions of the wave function given by Eqs. (30) and (33). This yields

$$p(R_0)=\frac{\sum_{E_{\lambda=0}<E_\lambda\leqslant E}p_\lambda(R_0)|F_\lambda(R_0)|^2}{\sum_{E_{\lambda=0}<E_\lambda\leqslant E}|F_\lambda(R_0)|^2}. \tag{34}$$

The value of $Z_{\rm eff}(R_0)$, which follows from Eqs. (31) and (34), varies from 5.08 a.u. at $E=1$ eV to 3.77 a.u. at $E=86$ eV with a maximum of 5.22 a.u. at $E=20$ eV. It thus remains close to the Wannier value of 4.95 a.u. throughout the energy domain investigated. This is why our final results vary by less than 1% when the parameter η in Eq. (32) varies from 10^2 to 10^{-4} a.u., enforcing the matching to the Wannier limit at 1 to 10^3 a.u. from R_0. Accordingly, we may consider our method as parameter free. The removal of the $\lambda=0$ component in Eq. (33), which was made possible by the already mentioned early decoupling of the channel associated to single ionization without excitation, definitely facilitates the definition of the unique local momentum $p(R)$. The neglect of the closed channels, which cannot be properly accomodated by the expression of Eq. (30), was required to avoid superfluous numerical noise.

Given the semiclassical ansatz of Eq. (30) and neglecting the inhomogeneous term, one can recast Eq. (17) into the form of a differential equation of first order with respect to R with the substitutions $\Phi(R;\Omega_5)\rightarrow\tilde{\Phi}(R;\Omega_5)$ and $\partial^2/\partial R^2 \rightarrow 2\imath p(R)\partial/\partial R-p^2(R)$. This implies that the term $p^{1/2}(R)\partial^2(p^{-1/2}(R)\tilde{\Phi}(R;\Omega_5))/\partial R^2$ has been neglected. The results presented below evidence that this approximation is of negligible consequence. Next, we introduce the mock time τ with the relation

$$Rp(R)d\tau=dR. \tag{35}$$

The substitution $Rp(R)\partial/\partial R\rightarrow\partial/\partial\tau$ allows us to rewrite the semiclassical equation of first order with respect to R as a conventional nonstationary Schrödinger equation with respect to the mock time. It is noteworthy that any term which does not depend on Ω_5 can be completely eliminated from this equation by a straightforward phase transformation. We then obtain the basic equation of our approach in the external region in the form

$$\imath\frac{\partial}{\partial\tau}\tilde{\Phi}(\tau;\Omega_5)=\left[\frac{1}{2}\frac{\mathcal{T}(\Omega_5)}{R(\tau)}+\mathcal{V}(\Omega_5)\right]\tilde{\Phi}(\tau;\Omega_5). \tag{36}$$

The latter deserves several comments. First, the dependence of $\tilde{\Phi}(R;\Omega_5)$ on the choice of $p(R)$ is only *implicit*. Second, the evolution of the system at large $R(\tau)$ consists in trivial

multiplication of the wave function by the phase factor generated by the potential operator $\mathcal{V}(\Omega_5)$.

We solve Eq. (36) using the split-operator method which is well known in contemporary nonstationary quantum mechanics [39]. It allows us to associate different types of propagators to different parts of the relevant Hamiltonian depending on their specifics. Here, we separate $\mathcal{U}_{ee}(\Omega_5)$ [see Eq. (20c)], which has a unique singular point ($\alpha=\pi/4, \theta_{12}=0$), from the rest of the Hamiltonian

$$\mathcal{H}(\tau;\Omega_5)=\frac{1}{2}\frac{\mathcal{T}(\Omega_5)}{R(\tau)}+\mathcal{U}_{en}(\alpha), \tag{37}$$

which has two lines of singularities at $\alpha=0$ and $\pi/2$, respectively. Then, we associate an exponential propagator to the operator that is the most regular, and a Crank-Nicholson [30] propagator to the singular most one. Accordingly, the elementary $\delta\tau$ propagation step consists of propagation over $\delta\tau/2$ with the Crank-Nicholson propagator related to $\mathcal{H}(\tau;\Omega_5)$, followed by propagation over $\delta\tau$ with the exponential of the operator $\mathcal{U}_{ee}(\Omega_5)$, and finally over $\delta\tau/2$ again with the Crank-Nicholson propagator associated with $\mathcal{H}(\tau;\Omega_5)$. The propagation operator over the elementary step $\delta\tau$ thus reads

$$\mathbf{P}_{\delta\tau}(\tau;\Omega_5)=\mathcal{P}_{\delta\tau/2}(\tau+\delta\tau/2;\Omega_5)\exp[-\imath\,\delta\tau\mathcal{U}_{ee}(\Omega_5)] \times\mathcal{P}_{\delta\tau/2}(\tau;\Omega_5)+\mathcal{O}(\delta\tau^3), \tag{38}$$

where

$$\mathcal{P}_{\delta\tau/2}(\tau;\Omega_5)=\left[1+\imath\frac{\delta\tau}{4}\mathcal{H}\left(\tau+\frac{\delta\tau}{4};\Omega_5\right)\right]^{-1} \times\left[1-\imath\frac{\delta\tau}{4}\mathcal{H}\left(\tau+\frac{\delta\tau}{4};\Omega_5\right)\right]. \tag{39}$$

Applying this operator step by step, one can, starting from the initial wave function, evaluate the wave function at arbitrary large τ and $R(\tau)$.

The implementation of this scheme requires us to choose a convenient representation of the various operators acting on the angular variables $(\alpha,\Omega_1,\Omega_2)$. In this respect, it is important to recall that the singular regions surrounding $\alpha=0$ and $\pi/2$, which correspond to single ionization with excitation, scale as $r_{n_{\max}}/R$, $r_{n_{\max}}$ being the extension of the highest Rydberg state excited. This makes these singularities much more difficult to handle in the outer region than in the inner region. Accordingly, the basis set representation of the variable α used in the inner region has to be abandoned in favor of a nonuniform grid representation with a high density of points in the vicinity of the singularities. On the other hand, the representation of the (Ω_1,Ω_2) variables based on the bipolar spherical harmonics $\mathcal{Y}^{1M}_{ll+1}(\Omega_1,\Omega_2)$ used in the inner region is retained in the outer region. Details are given in the Appendix. Here, we only wish to point out the contrasted properties of the resulting representations of $\mathcal{H}$ and $\mathcal{U}_{ee}$. Namely, the local potential $\mathcal{U}_{ee}$ is diagonal in α and in (g,u), whereas it couples different angular momenta $l\neq l'$. By contrast, $\mathcal{H}$ is diagonal in the basis of bipolar harmonics. Regarding α, $\mathcal{H}$ turns out to be tridiagonal, as we evaluate the second order derivative with respect to α that occurs in $\mathcal{T}(\Omega_5)$ using the three-point differentiation formula. These very different structures of the representations of $\mathcal{H}$ and $\mathcal{U}_{ee}$ confirm the relevance of the particular splitting we have chosen.

Let us now summarize the main advantages of our propagation scheme.

The first one is that this propagation scheme is computationaly *fast*. This is because the propagator associated with the τ-independent $e-e$ repulsion operator $\mathcal{U}_{ee}(\Omega_5)$ can be computed once and for all. And, also, because the evaluation of the τ-dependent Crank-Nicholson propagator amounts to the inversion of a tridiagonal matrix, a task which can be completed using a fast algorithm involving only $\mathcal{O}(N)$ multiplications, with N the dimension of the matrix [30]. In addition, the uniform mesh we use in the mock time corresponds to a quasiexponential mesh for the hyper-radius at large R, where $p(R)\simeq\sqrt{2E}$, so that $R(\tau)\simeq\exp(\tau\sqrt{2E})$. This allows a quick propagation of the system up to very large values of the hyper-radius, typically up to $R_{\max}=10^5$ a.u. in what follows.

The second advantage is that it is *explicitly unitary*. Namely, the Crank-Nicholson propagator is unitary by construction. Moreover, we calculate the representation of the exponential propagator as a series expansion in powers of the representation of $\mathcal{U}_{ee}$, a procedure which yields a unitary matrix to all orders. The unitarity of the full propagator follows. It guarantees the *explicit conservation of the total flux* throughout the external region. Accordingly, the total ionization cross section determined in the preceding section from the total flux at the border of the internal region [see Eq. (28)], is conserved by propagation.

Another advantage of our propagation scheme is that it allows one to visualize the evolution of the wave function from the boundary $R_0=10$ a.u., where it is formed, to $R_{\max}=10^5$ a.u., where the cross sections are extracted. This provides valuable physical information regarding the dynamics of the complex multichannel photoionization process considered. This peculiarity of our approach will be illustrated in the following section.

V. RESULTS

The absolute TDCS recorded by Braüning *et al.* [8] at 20 eV above threshold are arguably the best measurements with which the results of any emerging theory should be compared. This is due primarily to the absolute character of these measurements, which, additionally, cover a wide range of energy sharings and detection geometries. Yet the statistics of these measurements are rather poor.

These experiments were performed using a synchrotron radiation that was very close to full linear polarization ($S_1=0.98$). We present their results in comparison with our H$\mathcal{R}$M-SOW calculations using a reference system with the z axis along the direction of the photon beam, and the x axis along the main axis of polarization. The ejection direction $\hat{k}_1$ of electron 1 is then located by the angle $\theta_1=(\hat{x},\hat{k}_1)$, ranging

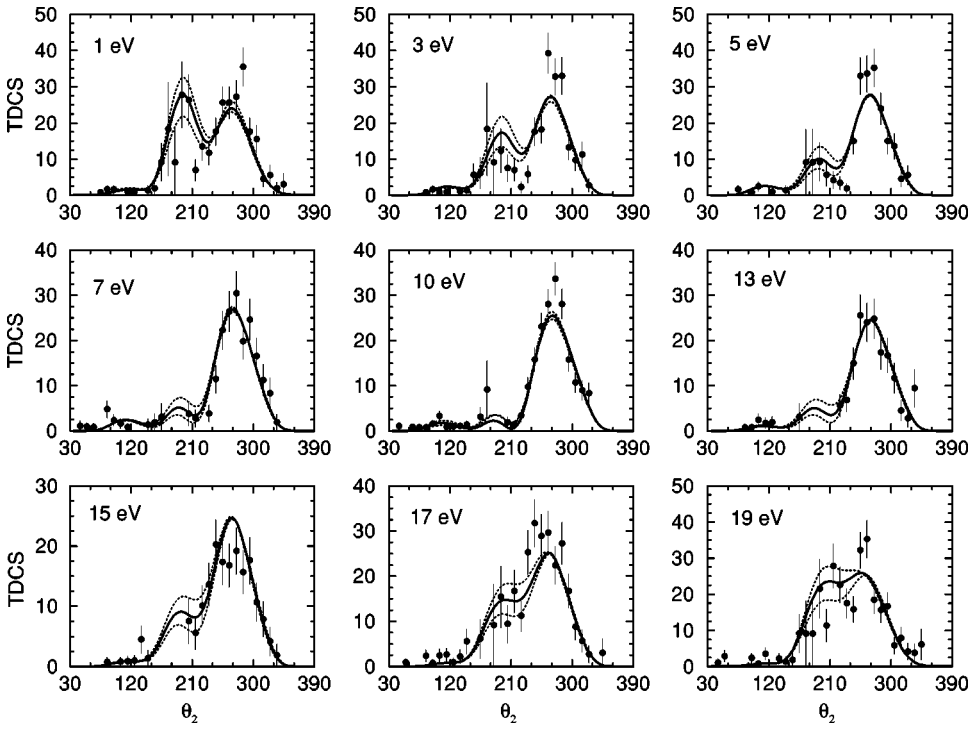

FIG. 2. TDCS at 20 eV above threshold in $b(eV)^{-1}(sr)^{-2}$ versus θ_2 in degrees for the geometry defined by $20° < \theta_1 < 40°$ and $0° < \phi_{12} < 20°$. The energy E_1 of the first electron is noted on each panel. Filled circles with error bars: measurements by Braüning *et al.* [8]. Thick solid line: present calculation for the energy E_1. Thin dotted lines: present calculations for the neighboring energies $E_1 + \Delta E_1/2$ and $E_1 - \Delta E_1/2$, as discussed in the text.

from 0 to 2π, in the $(\hat{x},\hat{k}_1)$ plane, and by the angle ϕ_1, ranging from 0 to π, between the $(\hat{x},\hat{y})$ and $(\hat{x},\hat{k}_1)$ planes. The same conventions are used for electron 2. Braüning *et al.*'s results were found to be rotationally invariant with respect to the main axis of polarization within experimental accuracy. The TDCS accordingly are considered as depending only on the difference, noted ϕ_{12}, between the angles ϕ_1 and ϕ_2, but not on the absolute values of these angles themselves. We have averaged our calculations over the finite angular sectors used by Braüning *et al.* in sorting their data, that is to say $\Delta\theta_1 = 20°$, and $\Delta\phi_{12} = 20°$. We have also illustrated the sensitivity of the results to the sharing of the energy between the two electrons by plotting together the TDCS corresponding to the three energies E_1, $E_1 - \Delta E_1/2$, and $E_1 + \Delta E_1/2$, which span the energy interval used by Braüning *et al.* to sort their data. The latter is $\Delta E_1 = 2$ eV at unequal energy sharing, and $\Delta E_1 = 4$ eV at equal sharing. A special situation occurs when $E_1 = 1$ eV and $E_1 = 19$ eV. At $E_1 = 1$ eV, we have not displayed the result for 0 eV, where single and double ionization cannot be disentangled, but for 0.1 eV. At $E_1 = 19$ eV, similarly, we have displayed the result for 19.9 eV instead of 20 eV.

Figure 2 illustrates the evolution of the TDCS with the energy ratio for a fixed geometry. It can be compared directly with Fig. 4 in Braüning *et al.*, where the measurements are displayed together with the associated CCC calculations. Regarding the shape of the TDCS, the overall agreement between our theory and experiment is good, as is good the agreement between CCC and experiment. In fact, the experiment is not accurate enough to allow the shape of the TDCS to decide between these two theories. However, the situation is quite different if one is interested in the absolute magnitude of the TDCS. In this respect, the very good agreement between the H$\mathcal{R}$M-SOW results and experiment should be appreciated keeping in mind that our approach does not involve any adjustable parameter, and that we have not applied any *a posteriori* rescaling factor to the raw results that come out of it. This contrasts with the CCC results, which had to be rescaled by the ratios of the SDCS expected on the basis of current experimental and theoretical knowledge to the raw SDCS obtained using CCC, before they could compare with experiment favorably as shown in Fig. 4 of [8]. These factors were 1.3, 0.75, 1.0, 1.5, and 2.3 for the energy pairs (1,19), (3,17), (5,15), (7,13), and (10,10), respectively [8]. Interestingly, Fig. 2 also shows that the sensitivity of the results to the energy ratio of the two electrons becomes more important with increasing asymmetry in the energy sharing.

Figure 3, which illustrates the evolution of the TDCS with the ejection direction of the first electron for three different energy ratios, can be compared directly with Figs. 3 and 5 of [8]. This comparison calls for the same remarks as those inspired by Fig. 2. Additionally, one can note that the sensitivity to the energy sharing is maximal when the first electron is emitted along the main axis of polarization, which makes this $\theta_1 = 0°$ geometry the most challenging for both theoreticians and experimentalists. It is worth noting that the TDCS obtained at $\theta_1 = 0°$ and $\theta_1 = 90°$ must be symmetric with respect to $\theta_1 = 180°$ and $\theta_1 = 270°$, respectively. The defect of symmetry in the angular pattern measured at $\theta_1 = 90°$ and $E_1 = 10$ eV, where the maximum of the right-hand-side lobe has no overlap with its left-hand-side counterpart, provides an interesting visualization of the statistical nature of the measurements. In the most challenging $\theta_1 = 0°$ geometry, unfortunately, Braüning *et al.* have chosen to improve the statistics by adding together the counts obtained at symmetric points with the counterpart that data are displayed in only one half plane. This makes the visual appreciation of the quality of the experiment more difficult. Our calculations for

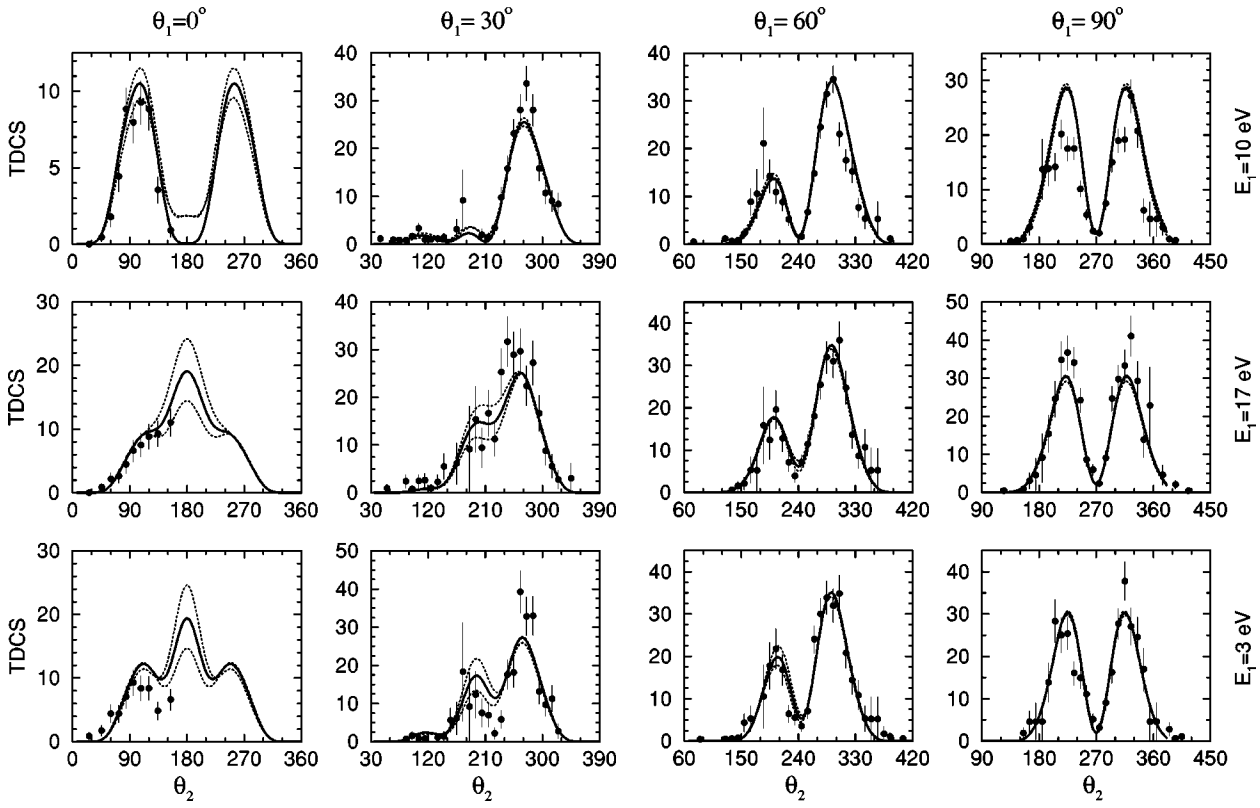

FIG. 3. TDCS at 20 eV above threshold in b(eV)$^{-1}$(sr)$^{-2}$ versus θ_2 in degrees. The geometrical arrangment is defined by $0°<\phi_{12}<20°$, for all panels, and by $350°<\theta_1<10°$, $20°<\theta_1<40°$, $50°<\theta_1<70°$, and $80°<\theta_1<100°$, for the panels in each column of the array of graphs, starting from the left, as indicated on the figure. Each line in the array of graphs corresponds to a given energy of the first electron: from top to bottom, $E_1=10$, 17, and 3 eV, as indicated on the figure. The other conventions are as in Fig. 2.

that case are given in the left column of Fig. 3.[2] Their agreement with experiment, which is very good at $E_1=10$ eV and $E_1=17$ eV, is surprisingly poor at $E_1=3$ eV. The CCC results for this geometry (see Fig. 5 of [8]), in contrast, agree well with experiment at $E_1=10$ eV and $E_1=3$ eV, but poorly at $E_1=17$ eV, despite the rescaling factor applied.

Integrating the TDCS over the direction of the second electron yields the DDCS defined by Eq. (11) above. The DDCS has a very simple angular structure which is described in linear polarization by

$$\frac{d^{(2)}\sigma}{dE_1 d\Omega_1}=\frac{1}{4\pi}\frac{d^{(1)}\sigma}{dE_1}[1+\beta P_2(\cos\vartheta_1)]. \qquad (40)$$

This expression is very similar to that of the differential cross section for single photoionization. However, in the above expression, the β parameter depends on the sharing of the energy between the two electrons, and not only on the total energy available above threshold. This parameter has no special behavior in the exchange of the energies of the two electrons: it is neither symmetric, nor antisymmetric. The β parameters computed under the assumption of full linear polarization are compared with the measurements by Wehlitz *et al.* [40], on top of Fig. 4. The agreement between theory and experiment, which is very good at 5, 10, and 21 eV excess energy, deteriorates at higher energies, where slight opposite-phase oscillations appear on the calculated and measured parameters, respectively. Surprisingly, only little attention has been paid to β by experimentalists up to now: namely, the dependence of β on the energy sharing has only been studied by Wehlitz *et al.* [40]. We hope that the structures that theory predicts in the dependence of β on the energy sharing will renew the interest of experimentalists in this quantity. Namely, more extensive experimental data are needed in order to ascertain the accuracy of the present calculations regarding β.

Integrating the DDCS with respect to the direction of the first electron yields the SDCS, also referred to as the energy-sharing cross section, a quantity that is well known to be invariant if the energies of the two electrons are interchanged. At the bottom of Fig. 4, we compare our SDCS with the absolute measurements by Wehlitz *et al.* [1]. The agreement between theory and experiment is excellent as far as the shape is concerned. The curves, which are very flat on the low-energy side, become more down convex at the highest excess energies, a trend that could already be observed on the 2SC calculations by Proulx and Shakeshaft [16]. It is worth to recall also that the equiprobability of all energy sharings was one conclusion of Wannier's threshold theory

[2]They differ from the ones shown in Figs. 1(d), 1(e), and 1(f) of [33] due to a missing factor 2 in Eq. (8) of [32], and to the physically inappropriate averaged momentum defined by Eq. (4) of [33].

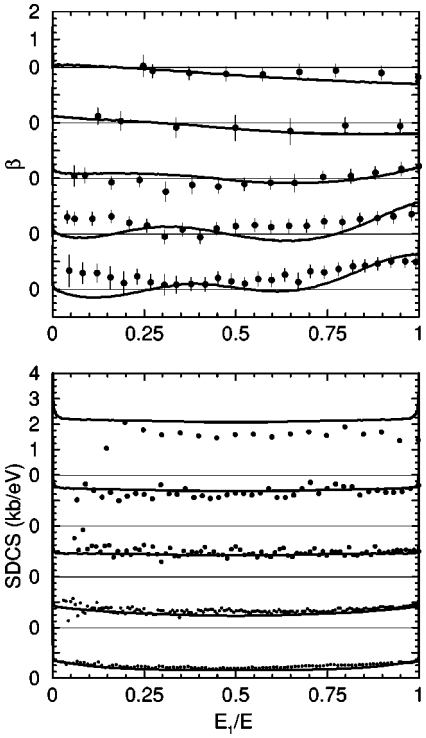

FIG. 4. Top panel: asymmetry parameter β versus the energy ratio E_1/E for five different excess energies above threshold: from top to bottom $E=5$, 10, 21, 31, and 41 eV. The thin horizontal lines give the zero of each β axis. The unique scale used can be read from the β axis above the highest zero line. Full circles with error bars: measurements by Wehlitz *et al.* [40]. Solid lines: present calculations. Bottom panel: SDCS in kb/eV versus the energy ratio E_1/E for the same excess energies as on the top panel. Full circles: measurements by Wehlitz *et al.* [1]. Solid lines: present calculations.

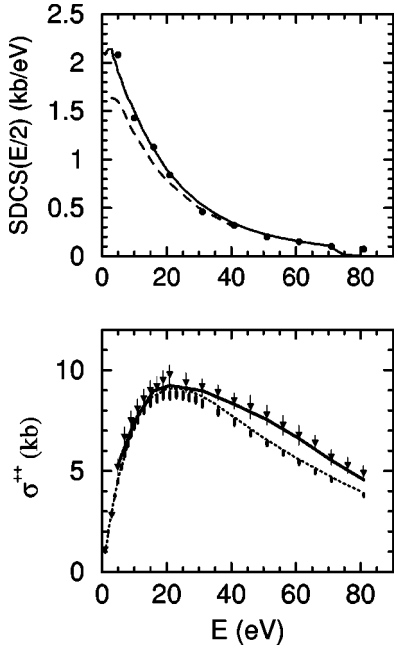

FIG. 5. Top panel: equal-energy sharing SDCS in kb/eV versus the total excess energy above threshold in eV. Filled circles: present calculation. Full line: 2SC calculation by Pont and Shakeshaft [17]. Dashed line: CCC calculation by Kheifets and Bray [43]. Bottom panel: integrated cross section for double photoionization, in kb, versus the total excess energy above threshold, in eV. Dots with error bars: experiment by Samson *et al.* [10]. Triangles down with error bars: experimental data compilation by Bizau and Wuillemier [34]. Dashed line: calculation by Pont and Shakeshaft [17]. Solid line: present calculations.

[23]. The SDCS computed using H$\mathcal{R}$M-SOW have huge structures around $E_1/E=0$ and 1, so narrow that they cannot be distinguished from the vertical axis at the scale of the figure, nor can they be resolved despite the very dense α grid used in these calculations. These structures correspond to single ionization to the excited ionic states. Turning now to the magnitude of the SDCS, we notice that the position of the computed curve relative to the experimental data evolves continuously with energy, being 30% too high at 5 eV, and a few percent too low at 41 eV. In this respect, it is important to recall that Wehlitz *et al.*'s data [1] were calibrated using the values of the total photoionization cross section compiled by Marr and West [41], which are now known to be overestimated by 9 to 16 % in the 5–41 eV range [4]. Recalibrating Wehlitz *et al.*'s data using Samson *et al.*'s more recent work would affect the comparison between these data and our calculations: the discrepancy would increase at low energy, but disappear at high energy, a situation that can be understood from Fig. 1 of the present paper and the associated comments.

We cannot abandon the subject of energy-sharing cross sections without contrasting the natural obtention of SDCS using H$\mathcal{R}$M-SOW with the intrinsic inability of CCC to produce reasonable approximations of these quantities. Namely, despite persevering efforts, the unphysical asymmetric and oscillating character of the SDCS obtained from CCC has not been remedied yet. The only improvement achieved concerns the value of the SDCS at equal energy sharing, which could be obtained, if one follows Stelbovics [42], by multipying the raw CCC value by a factor 4. The equal energy sharing SDCS obtained using this procedure [43] are compared on top of Fig. 5 with the present H$\mathcal{R}$M-SOW and 2SC calculations, respectively. These two latter theories agree very well with each other, whereas the CCC results lie slightly lower, the more so the lower the energy. This factor 4 thus seems to allow one to extract reasonable values of the equal-energy sharing SDCS from CCC calculations.

The natural way to compute the ICS for double photoionization is to substract the cross sections for single ionization to the ground and excited ionic states from the total ionization cross section given by Eq. (28). As this procedure does not require any explicit description of the double continuum, it is simple and accurate. Yet we prefer to compute the ICS by integrating the SDCS over the energy of the first electron, because our purpose here is to provide a complete check of the consistency of our method, the object of which is to cope with the double continuum. Performing this integration, which is defined by Eq. (14), requires to suppress the contributions of single ionization in some approximate way. To do that, we have found it convenient to replace the raw SDCS that comes out of our calculations by an even sixth-order

polynomial in the variable E_1-E, the coefficients of which are determined by matching to the original SDCS at four points. One of these points is $E_1=E/2$, and the three others are chosen to span the interval $]0,E/2[$ in such a way that the resulting polynomial can only be distinguished from the raw SDCS in the narrow singular regions around $E_1=0$ and $E_1=E$. The ICS we present are obtained by integrating these polynomial approximations from 0 to $E/2$. They are stable to within a few percent with respect to any reasonable change in the location of the matching points. Our results are compared at the bottom of Fig. 5 with the data compilation by Bizau and Wuillemier [34], and with the latest measurements by Samson *et al.* [10], which are systematically lower than the former. The discrepancy between these two sets of data, which reaches a maximum of the order of 15% around 50 eV excess energy, has not been fully explained yet. The H$\mathcal{R}$M-SOW calculations lie at the bottom of the error bars associated with the first set of data. The 2SC calculations by Pont and Shakeshaft [17], in contrast, are located at the top of the error bars associated with the second set of measurements. These two sets of experimental data will have to be reconciled somehow, and our approximate calculation of the ICS replaced by an explicit subtraction of the single-ionization channels, before this puzzling situation can be commented on any further.

As already noted, one advantage of our method is that it allows one to follow the evolution of the wave function throughout the external region. The following figures thus display, for various R values in the interval $[R_0,R_{\max}]$, the renormalized fluxes that converge at infinity to the TDCS, the DDCS, and the SDCS, respectively, according to Eqs. (10)–(12). We give them the same name as their respective asymptotic limits, although it is clearly an abuse of language. Note that the approximate procedure we use to compute the ICS becomes meaningless as R decreases, because the size $\Delta\alpha\simeq(0.75n_{\max}^2/R)$ rad of the singular regions associated with single ionization increases, untill it covers the entire α range from $R=100$ a.u. downwards. Accordingly, we do not present any R evolution of the ICS.

The left column and the right one in Fig. 6 display the same TDCS on different vertical scales. The scale used in the left column is appropriate for visualizing the patterns obtained at $R=R_0$. As they are still entangled with the dominant single-ionization channels, their absolute values are much higher than those of the TDCS to which they converge at large R. Their shapes result from the incomplete development of the electron-electron correlations, which makes it very likely for the two electrons to be observed in the same half plane, for instance. The scale used in the right column focuses on the evolution of the angular patterns from $R=10^2$ a.u. onwards. At equal energy sharing (see Fig. 6, middle line), the angular pattern extracted at $R=10^2$ a.u. is already in excellent agreement with the measured TDCS. In contrast, for the very asymmetric energy sharings (see Fig. 6, top and bottom lines), it is still very different from the experimental TDCS in shape as well as in magnitude: the relative heights of the two observed structures are wrong, and the absolute value is too high by as much as a factor 2. This

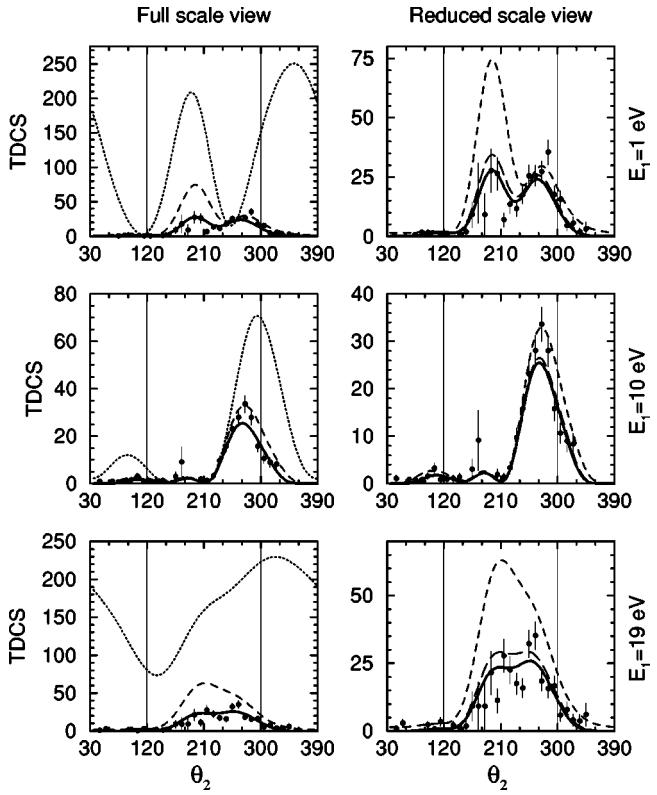

FIG. 6. TDCS at 20 eV above threshold, in b(eV)$^{-1}$(sr)$^{-2}$, versus θ_2 in degrees. The geometry is defined by $20°<\theta_1<40°$ and $0°<\phi_{12}<20°$. Each line in the array of graphs corresponds to a fixed energy of the first electron: from top to bottom, $E_1=1$, 10, and 19 eV, as indicated on the figure. The left and right columns in the array display the same results but on different vertical scales. Full circles with error bars: measurements by Braüning *et al.* [8]. Dotted lines: present calculations at $R=10$ a.u. Dashed lines: same at $R=100$ a.u. Long-dashed lines: same at $R=1000$ a.u. Thick solid lines: same at $R=10^5$ a.u. where convergence is reached. The angular range between the two vertical lines at $\theta_2=120°$ and 300° corresponds to emission of the two electrons in opposite half planes.

demonstrates the need to propagate at least up to $R=10^3$ a.u. in these particular dynamical situations.

Figure 7 illustrates the R evolution of the asymmetry parameter β at 21 eV excess energy. The curve obtained at $R=10^2$ a.u. still misses 5 experimental points in 14, whereas that extracted at $R=10^3$ a.u. misses only one, and so achieves an excellent agreement with experiment. This confirms the need to propagate up to thousands of atomic units away from the core, as already noted above.

Figure 8 shows the R evolution of the SDCS obtained at 21 eV excess energy. The vertical scale on the left panel is chosen to provide a full view of the pattern obtained at R_0. As R increases, the middle part of this pattern widens, flattens, and goes down, while the two side peaks get much narrower and higher, so that the total outgoing flux, represented by the area under the curve, remains constant. At $R=100$ a.u., the side peaks are already so narrow that they can hardly be distinguished from the vertical axis, and so high that their maxima are located far above the figure. In

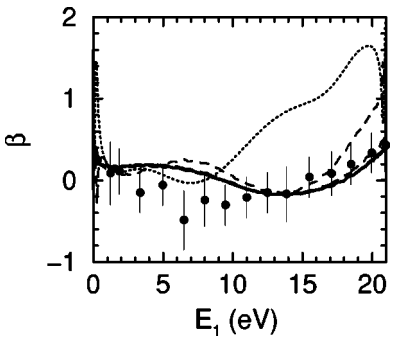

FIG. 7. Asymmetry parameter β at 21 eV above threshold versus the energy of one electron, in eV. Full circles with error bars: measurements by Wehlitz *et al.* [40]. The conventions for the lines are the same as in Fig. 6.

other words, with increasing R, flux is leaking out of the Wannier ridge $\alpha=\pi/4$ into the potential wells at $\alpha=0$ and $\pi/2$, thus ending in the single-ionization instead of in the double-ionization channel. The right panel concentrates on the evolution between $R=100$ a.u. and $R=1000$ a.u. The result obtained at $R=10^2$ a.u. is within 20% of the experimental value throughout most of the energy range available, excluding the neighborhood of the boundaries $E_1=0$ eV and $E_1=21$ eV. So, if one is interested in significantly asymmetric energy sharings or in a few percent accuracy, propagation up to $R=10^3$ a.u. is clearly required. The same conclusion was drawn before from the inspection of the TDCS and DDCS evolutions on Figs. 6 and 7.

VI. CONCLUSION

We have presented the H$\mathcal{R}$M-SOW method in detail. The central idea, which is to combine $\mathcal{R}$-matrix and semiclassical techniques within a hyperspherical coordinate system, is most likely open to other applications than the one reported on here. The method does not involve any adjustable parameter and so can be characterized as *ab initio*. It is accurate enough numerically to provide results that are gauge invariant to an excellent approximation.

We have displayed a wide selection of computed ionization cross sections, ranging from the fully differential to the fully integrated type, and regarding single- as well as double-ionization processes. The overall agreement between these data and the corresponding absolute measurements is very good, not only in shape, but also, more importantly, in magnitude. This demonstrates that the approximations entering the method, which is not formally exact, are well founded. H$\mathcal{R}$M-SOW thus emerges as a robust and reliable method.

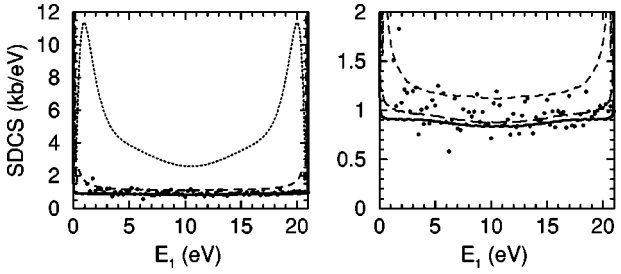

FIG. 8. SDCS at 21 eV above threshold, in kb/eV, versus the energy of one electron, in eV. The left and right panels display the same results but on different vertical scales. Full circles: measurements by Wehlitz *et al.* [1]. The conventions for the lines are the same as in Fig. 6.

The present calculations have been performed on a plain PC with 768 Mo RAM. This limited memory has prevented us from testing the convergence of our results as fully as we wished, namely, by increasing the dimensions of all representations involved in this six-dimensional problem *simultaneously*, and by taking a matching hyper-radius R_0 larger than 10 a.u. The very next step in the development of H$\mathcal{R}$M-SOW will therefore consist of implementing the codes on a powerful computer center, in order to get rid of memory-shortage problems, and to definitely assess the accuracy of the method in the various energy domains of interest. At this stage, the comparison with accurate relative TDCS measurements performed at intermediate energies under various well-defined conditions of polarization [11,12], as well as with absolute TDCS measurements at very low energies [13], will be particularly relevant.

As soon as its accuracy will have been characterized with confidence, H$\mathcal{R}$M-SOW will reveal its whole potential by providing, beyond the values of the measurable cross sections, valuable informations on the dynamics of the process that neither experiment nor other theories can reach directly to date. This gives H$\mathcal{R}$M-SOW a significant and distinctive advantage over other methods.

The gerade and ungerade complex amplitudes $\mathcal{M}^g(R_{\max};\alpha,\theta_{12})$ and $\mathcal{M}^u(R_{\max};\alpha,\theta_{12})$, for instance, are the elementary dynamical constituents of any double-photoionization cross section, and so, they contain complete information on the asymptotics of the process [44,12]. Yet these quantities have never been computed using an *ab initio* theory, and experiment can only provide indirect, partial, and moderatly accurate information about them. Therefore, it is worth to note that these amplitudes occur naturally in H$\mathcal{R}$M-SOW, which puts us in a position to obtain accurate representations of them in the near future, and so, to contribute to the current debate regarding their parametrization in a deciding way [45].

The R evolution of the structure of the total outgoing flux is a quantity that can hardly be an object of experimental study. Nevertheless, our knowledge of the dynamics of the process will remain incomplete as long as we will not have any reasonable idea of the way the total outgoing flux is redistributed over the final outgoing channels in the course of the system expansion. Yet such an idea can be obtained from H$\mathcal{R}$M-SOW, since this method allows one to follow the evolution of the photoabsorption wave function from the border of the inner region, where it is formed initially, up to the asymptotic region, where the measurements are performed. In this respect, the present paper already suggests that the very asymmetric energy sharing situations can only be handled if an accurate description of the system is available from the origin to thousands of atomic units from the core. It is worth to note that to date, our method is the only one that offers such a description.

ACKNOWLEDGMENTS

We are very grateful to T. Reddish for his comments on the manuscript and we thank R. Wehlitz for communicating his detailed data regarding β parameters to us.

APPENDIX: COMPUTATIONAL DETAILS

The numerical implementation of our approach relies upon specific representations of the relevant wave functions and operators. Below, we define these representations, and point out the dimensions they must be given in order to converge the calculation in the illustrative case of 20 eV above the He double-photoionization threshold.

Whatever the region considered, we use the same basis set representation of the dependence on the variables (Ω_1,Ω_2), based on the gerade and ungerade bipolar spherical harmonics,

$$ {}^{g}_{u}\mathcal{Y}^{1M}_{l,l+1}(\Omega_1,\Omega_2)=\frac{1}{\sqrt{2}}[\mathcal{Y}^{1M}_{l,l+1}(\Omega_1,\Omega_2)\pm\mathcal{Y}^{1M}_{l,l+1}(\Omega_2,\Omega_1)]. \tag{A1}$$

These functions, which are, respectively, symmetric (gerade) and antisymmetric (ungerade) in the exchange of Ω_1 and Ω_2, occur naturally in the construction of the ${}^1P^o_M$ two-electron orbital wave function produced by one-photon absorption from the He ground state. In Eq. (A1), l and $l+1$ are the angular momentum of the two electrons, and the bipolar spherical harmonics $\mathcal{Y}^{1M}_{l,l+1}(\Omega_1,\Omega_2)$ agree with the conventions used by Varshalovich *et al.* [36]. Our calculations were converged with $n_l=5$ harmonics in the inner region, and $n'_l=25$ harmonics in the outer region. This reflects the evolution of the two-electron wave function toward a product of two uncorrelated Coulomb waves, the partial-wave expansions of which are dominated at large distances by high angular momenta.

The representation of the dependence on the variable α has to meet higher requirements in the outer region compared to the inner region.

In the inner region, we use a basis set representation which is designed to comply with the requirements of (i) being composed of basis vectors that are either symmetric (gerade) or antisymmetric (ungerade) with respect to the exchange of the radial coordinates of the two electrons, that is to say with respect to the transformation $\alpha\rightarrow\pi/2-\alpha$; and (ii) being able to reproduce the behavior of the solution of Eqs. (21) and (23) at the boundaries of the α interval of variation. The analysis of the singularities of the kinetic-energy operator $\mathcal{T}(\Omega_5)$ shows that this behavior scales as α^{l+1} and $(\pi/2-\alpha)^{l+1}$ around $\alpha=0$ and $\pi/2$, respectively. The set

$$ {}^{g}\omega^{l}_{n}(\alpha)=(\sin\alpha\cos\alpha)^{l+1}\cos 4n\alpha, \quad n=0,\ldots,n_a-1, \tag{A2a}$$

$$ {}^{u}\omega^{l}_{n}(\alpha)=(\sin\alpha\cos\alpha)^{l}\sin 4n\alpha, \quad n=1,\ldots,n_a \tag{A2b}$$

is among the simplest possible choices. The $\cos 4n\alpha(\sin 4n\alpha)$ factors are the basis vectors of the Fourier expansion of a periodic function built from an even (odd) function defined on the interval $[0,\pi/2]$. The ${}^{g}_{u}\omega^{l}_{n}(\alpha)$ are orthonormalized within each subspace of given orbital angular momentum l and symmetry (g,u) to yield the final α basis set. Our calculations were found to converge with $n_a=40$ basis vectors.

In the outer region, we use the nonuniform grid representation defined by

$$ \alpha_k=\frac{\pi}{4}(1-\cos 2x_k), \quad x_k=\frac{\pi k}{2(n'_a+1)}, \quad k=1,\ldots,n'_a. \tag{A3}$$

The high density of points in the vicinity of $\alpha=0$ and $\pi/2$ allows us to describe accurately the behavior of the wave function in these regions, which correspond to one-electron ionization with excitation of the residual ion. The accuracy of the propagation scheme is guaranteed as long as the minimum α step, $\pi^3/[8(n'_a+1)^2]$, remains significantly smaller than the extension $r_{n_{\max}}/R$ of the singular regions mentioned above. Hence, a grid of dimension n'_a allows one to propagate up to $R_{\max}\ll 8r_{n_{\max}}(n'_a+1)^2/\pi^3$ that is to say $R_{\max}\simeq n'^2_a$, accordingly, the current paper was performed with $n'_a=100$ and $R_{\max}=10^4$, and we used $n'_a=1000$ and $R_{\max}=10^5$ for the final high-precision calculations.

The treatment of the hyper-radius R is very different in the inner and outer regions.

In the outer region, the propagation over the mock-time τ is based on a constant mock-time step $\delta\tau$ which is taken equal to 10^{-3} a.u. in all the present calculations. The R grid produced in propagation appears to be quasiexponential, as already noted in the text, which allows fast propagation to the very large distances where the two electrons correlation vanishes.

In the inner region, we use a Lagrange mesh representation of the reduced hyper-radius, $\rho=R/R_0$, defined on the interval $[0,1]$. This representation, which amounts to a particular case of DVR (discrete variable representation) [46], uses two related objects: (i) a grid of points, which consists in the zeros ρ_i, $i=0,\ldots,n_\rho$ of the Gegenbauer polynomials $G^{6,6}_{n_\rho}(\rho)$ [47]; and (ii) the basis of normalized Lagrange functions

$$ h_i(\rho)=\alpha_i\rho^{5/2}\frac{G^{6,6}_{n_\rho}(\rho)}{\rho-\rho_i},$$

$$ \alpha_i=(-1)^i\sqrt{\rho_i(1-\rho_i)}\,\frac{(2n_\rho+5)!}{n_\rho!(n_\rho+5)!}, \quad i=1,\ldots,n_\rho, \tag{A4}$$

which obey the orthonormalization condition

$$ \int_0^1 h^*_i(\rho)h_j(\rho)d\rho=\delta_{ij}, \tag{A5}$$

as well as the characteristic relation of Lagrange interpolation functions

$$h_i(\rho_j) = \lambda_i^{-1/2} \delta_{ij} . \tag{A6}$$

The λ_i are the weights of the Gaussian quadrature associated with the grid points ρ_i. The choice of this specific Lagrange-Gegenbauer mesh has been dictated by the physical boundary conditions at $\rho=0$ and 1. At $\rho=1$, the basis functions, or part of them at least, have to be nonzero to allow for some flux leaving the inner region. At $\rho=0$, they must be able to reproduce the behavior of the solutions of Eq. (21), which vanish at least as rapidly as $R^{7/2}$. In fact, the practical resolution of Eq. (21) on the Lagrange mesh implies premultiplying this equation by R and introducing the reduced function $\Phi^k(R,\Omega_5)/R$ [48]: therefore, the $\rho^{5/2}$ behavior of the basis functions given by Eq. (A4) is adapted to the description of the reduced function. Given $R_0=10$ a.u., a 15 point mesh has proved sufficient to converge our calculations.

It is instructive to present a few orders of magnitude to help the reader appreciate the weight of the computational task. The dimension of the representation used to solve Eq. (21) is $2\times n_l \times n_a \times n_\rho$, so that, at convergence, a 6000 $\times$6000 matrix has to be stored and diagonalized. The dimension of the vector to propagate in the outer region is $2\times n_l' \times n_a'$, which reaches 50 000 for high-precision calculations. Finally, about 7000 elementary mock-time steps $\delta\tau = 10^{-3}$ a.u. are needed to propagate the wave function from $R_0=10$ a.u. to $R_{\max}=10^5$ a.u.

The computation of the matrix elements of the various operators within the representations given above is straightforward. Nevertheless, it is worth mentioning that (i) the integrations over Ω_1 and Ω_2 are performed exactly using standard Racah algebra; (ii) the integrations over α are performed exactly using either exact Gaussian quadratures or the residues theorem; and (iii) the integrations over ρ are performed exactly using the Gaussian quadrature associated with the mesh. Indeed the latter leads to compact exact analytical expressions of the potential- and kinetic-energy operators, following the distinctive property of Lagrange meshes [49].

We can thus state that, within the representation described above, the computation of the $\mathcal{R}$-matrix eigenvectors from Eq. (21) is exact. A consequence of this exactness is the excellent accuracy of our calculation of the energies of selected $^1P^o$ bound states of He, already mentioned in the text.

In the outer region, the accuracy of the grid representation used for the variable α could be questioned given the strong singularities of the potential at $\alpha=0$ and $\pi/2$, and the limited precision of the three-point differentiation formula used to evaluate the second-order derivative with respect to α. However, test calculations with $n_a'=3000$ mesh points have confirmed that the results presented in this paper, which have been obtained with $n_a'=1000$ mesh points, are converged to better than 1% with respect to n_a'. This illustrates well the advantages of using a nonuniform grid adapted to the local rate of variation of the wave function considered.

In the present version of our codes, we have described the ground state of He by the 20 terms Hylleraas-type wave function of Hart and Herzberg [50]. It follows that the projections of the inhomogeneous term $\Phi^G(R;\Omega_5)$ on the $\mathcal{R}$-matrix eigenvectors $\Phi^k(R;\Omega_5)$ can only be obtained by a threefold numerical integration, which turns out to be very accurate although not formally exact. In the future, we plan to use the He ground-state wave function obtained by solving Eqs. (24) and (25), with the inhomogeneous term suppressed, within a $^1S^e$ representation akin to the $^1P^o$ one used presently for computing the wave function of the photoabsorption state. The computation of the projections will then be quick and exact.

[1] R. Wehlitz, F. Heiser, O. Hemmers, B. Langer, A. Menzel, and U. Becker, Phys. Rev. Lett. **67**, 3764 (1991).

[2] O. Schwarzkopf, B. Krässig, J. Elmiger, and V. Schmidt, Phys. Rev. Lett. **70**, 3008 (1993).

[3] A. Huetz, P. Lablanquie, L. Andric, P. Selles, and J. Mazeau, J. Phys. B **27**, L13 (1994).

[4] J. A. R. Samson, Z. X. He, L. Yin, and G. N. Haddad, J. Phys. B **27**, 887 (1994).

[5] O. Schwarzkopf and V. Schmidt, J. Phys. B **28**, 2847 (1995).

[6] P. Lablanquie, J. Mazeau, L. Andric, P. Selles, and A. Huetz, Phys. Rev. Lett. **74**, 2192 (1995).

[7] G. Dawber, L. Avaldi, A. G. McConkey, H. Rojas, M. A. McDonald, and G. C. King, J. Phys. B **28**, L271 (1995).

[8] H. Bräuning, R. Dörner, C. L. Cocke, M. H. Prior, B. Krässig, A. S. Kheifets, I. Bray, A. Bräuning-Demian, K. Carnes, S. Dreuil, V. Mergel, P. Richard, J. Ullrich, and H. Schmidt-Böcking, J. Phys. B **31**, 5149 (1998).

[9] V. Mergel, M. Achler, R. Dörner, Kh. Khayyat, T. Kambara, Y. Awaya, V. Zoran, B. Nyström, L. Spielberger, J. H. McGuire, J. Feagin, J. Berakdar, Y. Azuma, and H. Schmidt-Böcking, Phys. Rev. Lett. **80**, 5301 (1998).

[10] J. A. R. Samson, W. C. Stolte, Z. X. He, J. N. Cutler, and Y. Lu, Phys. Rev. A **57**, 1906 (1998).

[11] J. P. Wightman, S. Cvejanović, and T. J. Reddish, J. Phys. B **31**, 1753 (1998).

[12] K. Soejima, A. Danjo, K. Okuno, and A. Yagishita, Phys. Rev. Lett. **83**, 1546 (1999).

[13] A. Huetz and J. Mazeau, Phys. Rev. Lett. **85**, 530 (2000).

[14] M. Brauner, J. S. Briggs, and H. Klar, J. Phys. B **22**, 2265 (1989); F. Maulbetsch and J. S. Briggs, *ibid.* **26**, 1679 (1993); J. Berakdar and J. S. Briggs, Phys. Rev. Lett. **72**, 3799 (1994).

[15] I. Bray and A. T. Stelbovics, Phys. Rev. A **46**, 6995 (1992); I. Bray and D. V. Fursa, *ibid.* **54**, 2991 (1996); I. Bray, Phys. Rev. Lett. **78**, 4721 (1997); A. Kheifets and I. Bray, J. Phys. B **31**, L447 (1998).

[16] D. Proulx and R. Shakeshaft, Phys. Rev. A **48**, R875 (1993).

[17] M. Pont and R. Shakeshaft, J. Phys. B **28**, L571 (1995).

[18] M. Pont, R. Shakeshaft, F. Maulbetsch, and J. S. Briggs, Phys. Rev. A **53**, 3671 (1996).

[19] A. K. Kazansky and V. N. Ostrovsky, J. Phys. B **27**, 447

(1994); **28**, 1453 (1995); Phys. Rev. A **51**, 3712 (1995); **52**, 1775 (1995); J. Phys. B **30**, 921 (1997).
[20] M. S. Pindzola and F. Robicheaux, Phys. Rev. A **57**, 318 (1998).
[21] J. Colgan, M. S. Pindzola, and F. Robicheaux, J. Phys. B **34**, L457 (2001).
[22] T. N. Rescigno, M. Baertschy, W. A. Isaacs, and C. W. McCurdy, Science **286**, 2474 (1999).
[23] G. H. Wannier, Phys. Rev. **90**, 817 (1953).
[24] I. Vinkalns and M. Gailitis, in *Proceedings of the 5th International Conference on Physics of Electronic and Atomic Collisions* (Nauka, Leningrad, 1967), Abstracts pp. 648–650; *Scattering of Electrons on Atoms* (Zinatne, Riga, 1967), pp. 17–34.
[25] R. Peterkop, J. Phys. B **4**, 513 (1971); **16**, L587 (1983).
[26] A. R. P. Rau, Phys. Rev. A **4**, 207 (1971); J. Phys. B **9**, L283 (1976).
[27] J. M. Feagin, J. Phys. B **17**, 2433 (1984); **29**, L551 (1996).
[28] T. N. Rescigno, C. W. McCurdy, W. A. Isaacs, and M. Baertschy, Phys. Rev. A **60**, 3740 (1999).
[29] J. S. Briggs and V. Schmidt, J. Phys. B **33**, R1 (2000).
[30] W. H. Press, S. A. Teulkolsky, W. T. Vetterling, and B. P. Flannery, *Numerical Recipes in Fortran (The Art of Scientific Computing)* (Cambridge University Press, Cambridge, 1994).
[31] P. G. Burke and W. D. Robb, Adv. At. Mol. Phys. **11**, 143 (1975).
[32] L. Malegat, P. Selles, and A. Kazansky, Phys. Rev. A **60**, 3667 (1999).
[33] L. Malegat, P. Selles, and A. Kazansky, Phys. Rev. Lett. **85**, 4450 (2000).
[34] J. M. Bizau and F. J. Wuillemier, J. Electron Spectrosc. Relat. Phenom. **71**, 205 (1995).
[35] M. Le Dourneuf, Vo Ky Lan, and J. M. Launay, J. Phys. B **15**, L685 (1982).
[36] D. A. Varshalovich, A. N. Moskalev, and V. K. Khersonskii, *Quantum Theory of Angular Momentum* (World Scientific, Singapore, 1988).
[37] D. Baye and P. H. Heenen, J. Phys. A **19**, 2041 (1986).
[38] S. Bashkin and J. O. Stoner, *Atomic Energy Levels and Grotrian Diagrams* (North-Holland, Amsterdam, 1975).
[39] M. D. Feit and J. A. Fleck, J. Chem. Phys. **78**, 301 (1982); **80**, 2578 (1984); M. D. Feit, J. A. Fleck, and A. Steiger, J. Comp. Physiol. **47**, 412 (1982).
[40] R. Wehlitz (private communication) based on the measurements reported in R. Wehlitz, F. Heiser, O. Hemmers, B. Langer, A. Menzel, and U. Becker, Phys. Rev. Lett. **67**, 3764 (1991).
[41] G. V. Marr and J. B. West, At. Data Nucl. Data Tables **18**, 497 (1976).
[42] A. T. Stelbovics, Phys. Rev. Lett. **83**, 1570 (1999).
[43] A. S. Kheifets and I. Bray, Phys. Rev. A **62**, 065402 (2000).
[44] L. Malegat, P. Selles, and A. Huetz, J. Phys. B **30**, 251 (1997); L. Malegat, P. Selles, P. Lablanquie, J. Mazeau, and A. Huetz, *ibid.* **30**, 263 (1997).
[45] S. Cvejanović and T. J. Reddish, J. Phys. B **33**, 4691 (2000).
[46] J. C. Light, I. P. Hamilton, and J. V. Lill, J. Chem. Phys. **82**, 1400 (1985).
[47] M. Abramowitz and I. Stegun, *Handbook of Mathematical Functions* (Dover, New York, 1972).
[48] M. Vincke, L. Malegat, and D. Baye, J. Phys. B **26**, 811 (1993).
[49] L. Malegat and M. Vincke, J. Phys. B **27**, 645 (1994).
[50] J. F. Hart and G. Herzberg, Phys. Rev. **106**, 79 (1957).